Ultramicroscopy 147 (2014) 8–20

Contents lists available at ScienceDirect

Ultramicroscopy

journal homepage: www.elsevier.com/locate/ultramic

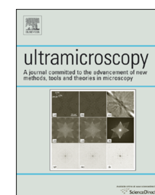

Determining the thickness of atomically thin MoS_2 and WS_2 in the TEM

Ryan J. Wu, Michael L. Odlyzko, K. Andre Mkhoyan *

Department of Chemical Engineering and Materials Science, University of Minnesota, Minneapolis, Minnesota 55455, USA

ARTICLE INFO

Article history:
Received 26 January 2014
Received in revised form
26 April 2014
Accepted 24 May 2014
Available online 2 June 2014

Keywords:
ADF-STEM
SAED
Thickness
MoS_2
WS_2
Tilt

ABSTRACT

Multislice simulations were used to analyze the reliability of annular dark field scanning transmission electron microscopy (ADF-STEM) imaging and selected-area electron diffraction (SAED) for determining the thicknesses of MoS_2 and WS_2 specimens in the aberration-corrected TEM. Samples of 1 to 4 layers in thickness for both 2H and 1T polymorphs were studied and tilts up to 500 mrad off of the [0001] zone axis were considered. All thicknesses including the monolayer showed distortions and intensity variations in their ADF-STEM images and SAED patterns as a result of tilt. Both techniques proved to be applicable to distinguish monolayers from multilayers using tilt. Without tilt, neither technique allows unambiguous thickness determination solely by comparing relative intensities of atomic columns in ADF-STEM images or diffraction patterns oriented along at [0001] zone axis, with the exception of monolayer 2H WS_2. However, differentiation is possible using absolute intensities in ADF-STEM images. The analysis of ADF-STEM images and SAED patterns also allows identification of the 2H and 1T polymorphs of MoS_2 and WS_2.

© 2014 Elsevier B.V. All rights reserved.

1. Introduction

Two-dimensional (2D) materials have been subject of an immense research effort in recent years. Since the isolation of graphene and recognition of its potential [1], the scientific community has actively studied these atomically thin materials for applications in electronics, mechanics, and optics [2,3]. Transition metal dichalcogenides (TMDs) with formula MX_2, where M is a transition metal and X is a chalcogen, form a unique class of layered materials distinct from that of graphene and hexagonal boron nitride (h-BN) [4,5]. Although the strong intraplanar covalent bonds coupled with weak interlayer van der Waals interactions that are characteristic of other 2D materials still persist, stable monolayers of TMDs do not exist as single atomic planes but as triplanar X–M–X stacked structures. This structural arrangement produces distinctive behavior in TMD monolayers, such as a band structure ranging from semiconducting for MoS_2 [6] and WS_2 [7] to metallic for $NbSe_2$ and $TaSe_2$ [8]. This diversity opens a host of applications for TMDs and shows their promise as building blocks for future devices.

Numerous characterization methods [9–11] have been used to study the structure and properties of TMD monolayers in much the same manner as other 2D materials. The transmission electron microscope (TEM), in particular, has proven to be an excellent tool for characterizing nano- and sub-nano-sized samples, especially since the introduction of aberration-corrected electron optics [12–14]. Scanning TEM (STEM), bright-field conventional TEM (BF-CTEM) and selected area electron diffraction (SAED) have all been employed in the study of TMD's atomic structure [4], grain boundaries [15], point defects [16] and susceptibility to electron beam damage [17]. Most TEM studies of TMDs are supplemented by atomic force microscopy (AFM) to provide direct thickness measurements. However, the low throughput of AFM, potentially small lateral size of TMD flakes and the challenges of transferring the samples onto a TEM grid make direct TEM-based determination of specimen thickness highly desirable [18].

One TEM-based method is to observe the intensity variations during SAED tilting, as experimentally demonstrated on MoS_2 by Brivio et al. [19] for differentiating monolayers from multilayers. Another method analyzes the column-to-column intensity ratio of metal and chalcogen sites in annular dark field STEM (ADF-STEM) images [20]; the latter method has also been demonstrated to distinguish between the 2H and 1T polymorphs of MoS_2 [21]. In addition, quantitative STEM has also been used to distinguish a 2H MoS_2 monolayer from a bilayer [22]. Other more common TEM techniques that have been used to measure thickness of materials include analysis of converged beam electron diffraction (CBED) zero-disk fringes [23–25] and low-loss electron-energy loss spectroscopy (EELS) [26–28]. To the best of our knowledge, no experimental evidence has shown these techniques to be suitable for TMDs and, therefore, they are not considered here.

This study analyzes the reliability of ADF-STEM imaging and SAED in determining the thicknesses of TMDs samples up to four layers through simulated TEM images and diffraction patterns.

* Corresponding author. Tel.: +1 6126252059; fax: +1 6126267246.
E-mail address: mkhoyan@umn.edu (K.A. Mkhoyan).

http://dx.doi.org/10.1016/j.ultramic.2014.05.007
0304-3991/© 2014 Elsevier B.V. All rights reserved.

Odlyzko and Mkhoyan [29] earlier concluded in a similar study of h-BN that BF-CTEM is not a reliable method for thickness determination and, therefore, a further application of BF-CTEM to TMDs is not pursued here. 2H MoS_2 and WS_2, as representative TMDs, are considered in this study along with their respective 1T polymorphs. Here the effects of tilt off of the [0001] zone axis on ADF-STEM images and SAED patterns are considered in order to determine suitable methods to measure the thickness of free-standing MoS_2 and WS_2.

2. Methods

ADF-STEM images and SAED patterns of 1–4 layer MoS_2 and WS_2 samples were simulated using the multislice method [30] implemented with the code developed by Kirkland [31]. A tilt series beginning at the [0001] zone axis was simulated in steps of 10 mrads or larger, up to 500 mrad off-axis. All simulations were performed for TEM operating with 200 kV, an accelerating voltage at which experiments on MoS_2 and WS_2 have been effectively performed with minimal beam damage [19,32,33]. The lattice parameters of MoS_2 and WS_2 with hexagonal crystal structure used were a=3.17 Å and c=6.14 Å, in accordance with experimentally and theoretically determined values [34,35].

ADF-STEM image simulations were performed using an aberration-corrected probe with $Cs_{(3)} = -0.041$ mm, $Cs_{(5)} = 5$ mm, $\Delta f = -35$ Å, and α_{obj}=20 mrad. These parameters were selected to reflect observed practical experimental probe characteristics at this electron beam energy, but without explicitly taking into account a finite source size or chromatic aberration of the microscope. The simulated beam has a full-width half-maximum (FWHM) of about 0.9 Å, which corresponds to a probe size slightly larger than that experimentally demonstrated at this energy [36]. Image simulations were performed on a 31 × 30 $Å^2$ supercell using a transmission function (TF) and probe function (PF) calculated at 1024 × 1024 pixelation. Slice thickness was set as $z = c * \cos(\theta_t)/4$, where θ_t represents the tilt angle, to maintain a similar number of atoms in each slice and to preserve the real z-direction spacing between the atoms throughout the tilt series. A simulated ADF detector collected electrons scattered 54–340 mrad off of the optic axis to form the image. Effects of thermal displacements were simulated by averaging 10 frozen phonons configurations at 300 K for each image (additional simulations showed that higher phonon configurations affected negligibly the ADF-STEM image considered here). Root mean square (rms) thermal displacement values used were 0.071 Å and 0.045 Å, for sulfur (S) and molybdenium (Mo), respectively [37,38]. The rms value of 0.023 Å for tungsten (W) was scaled from Mo according to the atomic mass ratio.

SAED pattern simulations were performed on a 252 × 252 $Å^2$ supercell using a slightly converged (1.5 mrad) beam to improve pattern visibility. As shown by Odlyzko and Mkhoyan [29], the results are quantitatively equivalent for convergence angles 0.25–2.00 mrads. TF and PF were calculated at 2048 × 2048 pixelation. Thermal effects were neglected in these sets of calculations since phonons only weakly dampen diffraction spots at 300 K for atomic vibrations with rms values of 0.1 Å and smaller [39]. All SAED patterns presented here are normalized to the most intense diffraction spot (saturating the central beam) and displayed using linear intensity scaling in each individual pattern.

The atomic structures of 2H and 1T MoS_2/WS_2 are shown in Fig. 1 along with the tilt axes. The x- and y-tilts were performed as rotations around the y- and x-axis, respectively, or around the $[\bar{1}2\bar{1}0]$ and $[10\bar{1}0]$ directions in a hexagonal lattice, respectively. Any arbitrary tilt direction can be represented as a superposition of tilts about these two axes.

3. Results

The results of ADF-STEM image and SAED pattern simulations for both 2H and 1T polymorphs of MoS_2 and WS_2 are shown and discussed separately below. Detectable tilt effects exist at every simulated thickness for both polymorphs of each material.

3.1. ADF-STEM Imaging for 2H MoS_2 and WS_2

The ADF-STEM image tilt series for 1 to 4 layers of 2H MoS_2 and 2H WS_2 are shown in Figs. 2 and 3, respectively. At the exact [0001] zone axis (0 mrad tilt), two sites with distinct intensities can be identified: the M-site corresponds to a position where the incident beam contacts a M atom first, and the X-site to a position where the incident beam contacts a X atom first (Fig. 1(c)). Fig. 4 shows the ADF intensity ratios of the peak intensity at the X-site to that at the M-site for each thickness. Despite the simulated beam having passed through the same number of M and X atoms at each site in even-layered samples, there is no intensity symmetry, which differentiates the case of 2H MoS_2/WS_2 from that of h-BN. The X/M intensity ratio at the monolayer is smaller for WS_2 than

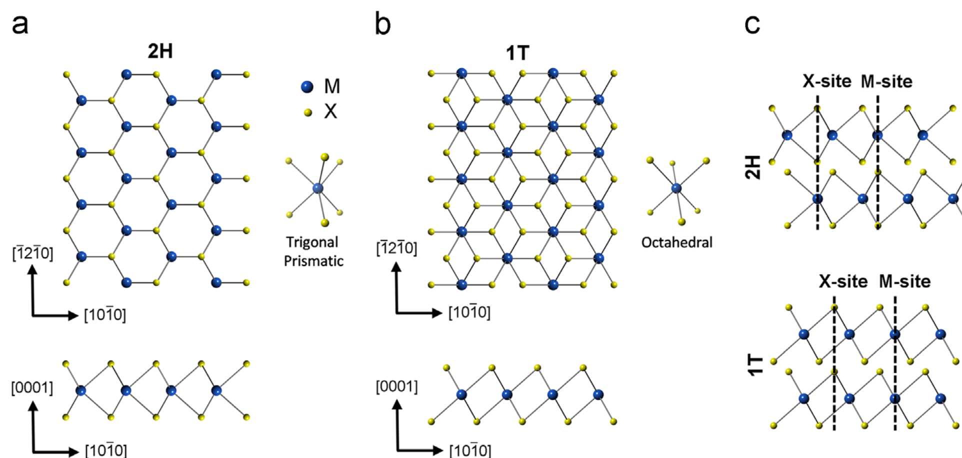

Fig. 1. Structural models of single layer 2H and 1T MX_2 crystals, where M is a Mo or W site and X is a S site, and tilt conventions. (a): 2H MX_2 structure; (top) [0001] view and (bottom) $[\bar{1}2\bar{1}0]$ view. (b): 1T MX_2 structure; (top) [0001] view and (bottom) $[\bar{1}2\bar{1}0]$ view. x-tilt corresponds to a rotation around the $[\bar{1}2\bar{1}0]$ axis and y-tilt corresponds to a rotation around the $[10\bar{1}0]$ axis. (c) Stacking of 2H and 1T MX_2 layers with M- and X-site convention.

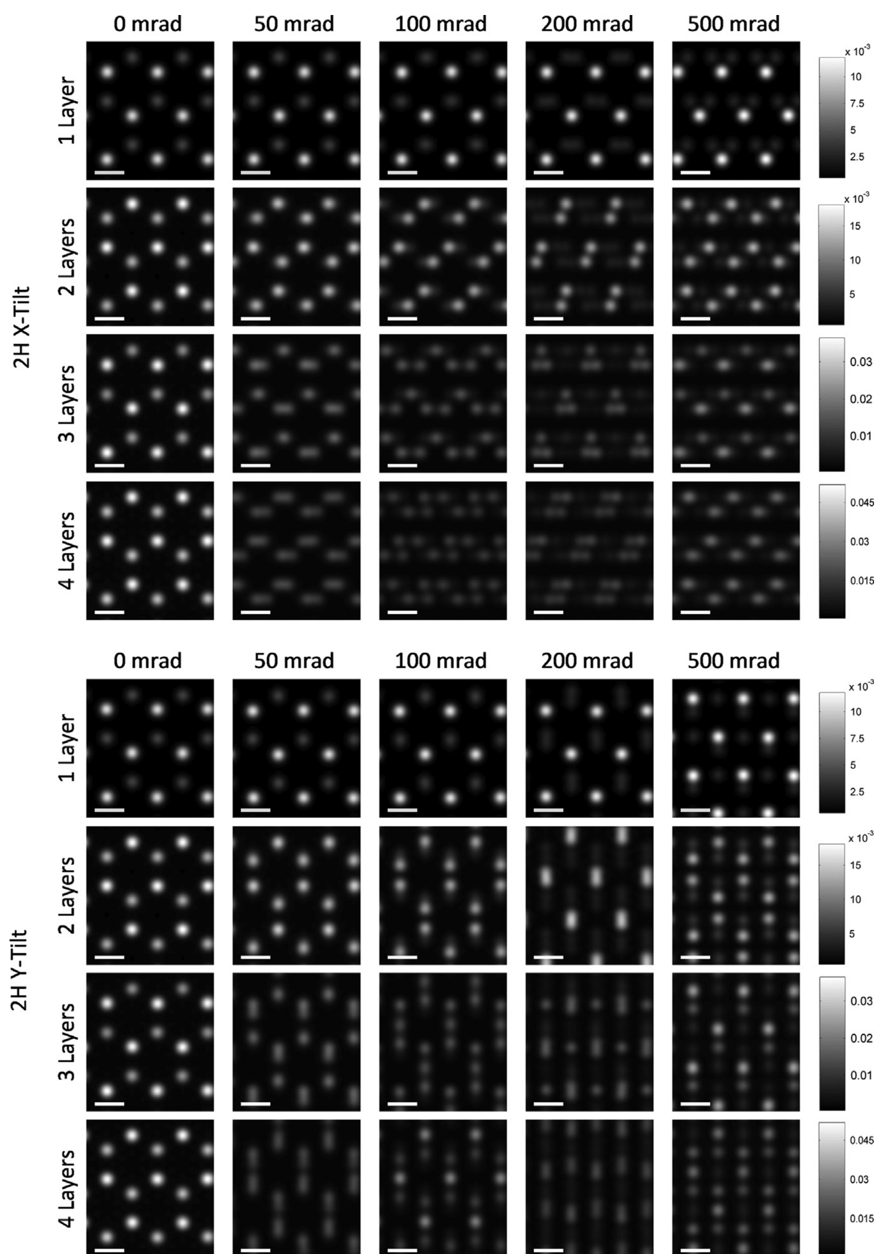

Fig. 2. Simulated ADF-STEM images of 2H MoS_2 at various *x*- and *y*-tilt angles. Both tilt directions produce unique intensity patterns at all thicknesses as a result of overlapping of Mo and S atoms. Color bars are scaled to each row with intensities normalized to the incident beam; scale bars are 1.8 Å.

MoS_2, which is expected from the atomic number (Z) dependence of incoherent high-angle scattering. Tilting multilayers beyond 50 mrad ($\sim 3^{\circ}$) in either direction creates distortions in the direction perpendicular to the tilt axis; these distorted patterns are easily distinguishable.

3.2. *ADF-STEM Imaging for 1T MoS_2 and WS_2*

Figs. 5 and 6 contain the simulated ADF-STEM images for 1T MoS_2 and 1T WS_2, respectively. In contrast to the 2H configuration, ADF-STEM images of 1T polymorph samples at [0001] zone axis appear very similar for all thicknesses. Since the M- and X-sites contain only their respective atoms for any number of layers in this configuration, the X-site/M-site ADF intensity ratio remains nearly constant for all thicknesses (see Fig. 4). The X-site/M-site ADF intensity ratios are smaller for WS_2 relative to MoS_2 as expected due to Z-dependence. Tilt effects in either direction begin to be distinguishable at 50 to 100 mrad, especially for the higher intensity M-sites. Additional tilt leads to complex effects such as M- and X-site overlaps for 2–4 layers similar to the 2H configuration.

3.3. *SAED characterization for 2H MoS_2 and WS_2*

The simulated SAED $\{10\bar{1}0\}$ spots at [0001] zone axis show comparable intensities at each thickness allowing easy identification of the honeycomb reciprocal lattice structure of 2H MoS_2 and WS_2 regardless of the number of layers. This is evident in the SAED simulations for 2H MoS_2 as shown in Fig. 7. 2H WS_2 SAED tilt series (not presented here) showed no qualitative differences from the 2H MoS_2 results. SAED simulations also indicate that both the

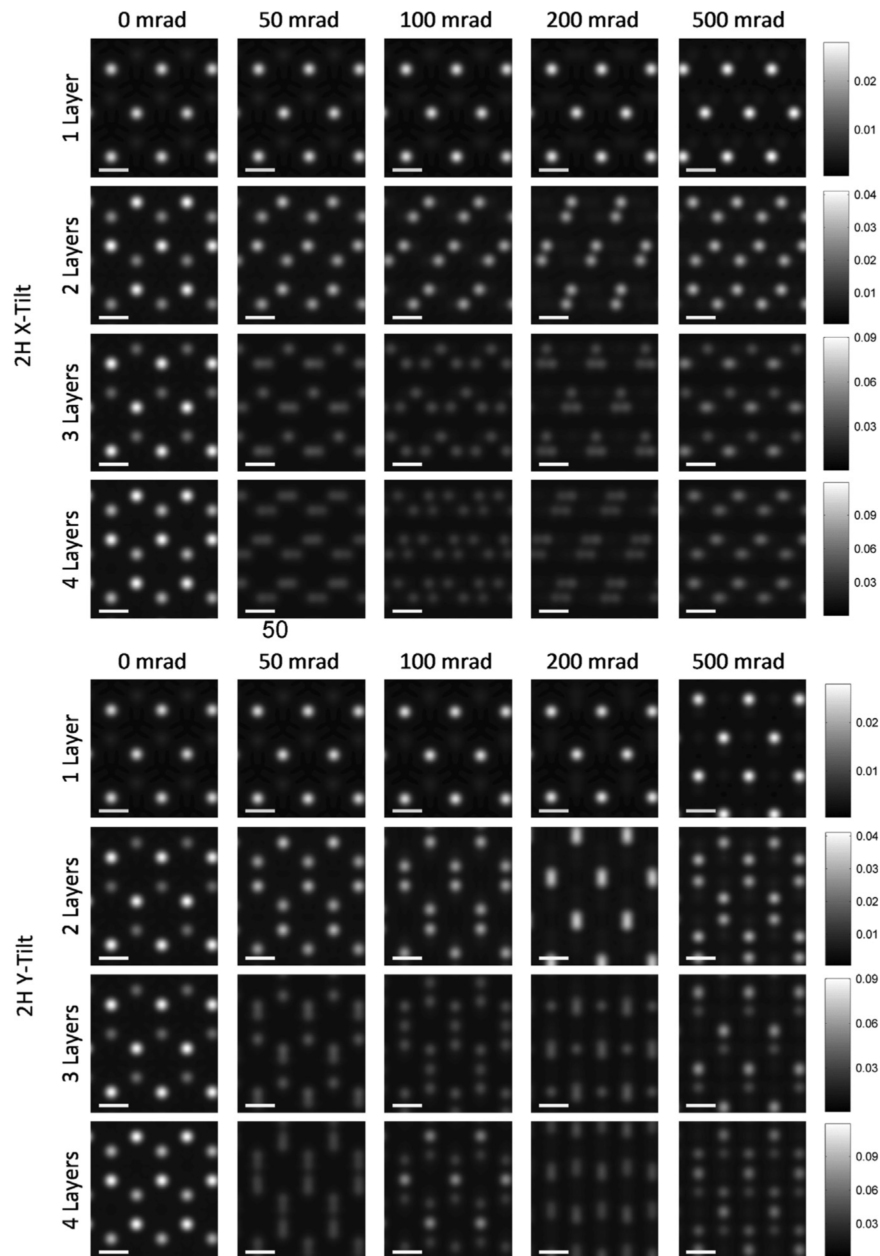

Fig. 3. Simulated ADF-STEM images of 2H WS_2 at various *x*- and *y*-tilt angles. Both tilt directions produce unique intensity patterns at all thicknesses as a result of overlapping of W and S atoms. Color bars are scaled to each row with intensities normalized to the incident beam; scale bars are 1.8 Å.

$\{10\overline{1}0\}$ and $\{11\overline{2}0\}$ spots are affected by *x* and *y*-tilt for all four thicknesses including the monolayer.

3.4. SAED characterization for 1T MoS_2 and WS_2

Thickness identification of 1T structures through SAED pattern analysis becomes challenging as the intensities of diffraction spots vary non-intuitively with tilt off of [0001] at all thicknesses. Fig. 8 shows the simulated SAED patterns for 1T MoS_2 and shows a hexagonal array of diffraction spots that oscillate asymmetrically about the *y*-axis during *x*-tilt, and oscillate symmetrically about the *x*-axis during *y*-tilt. This arises from the structure of $\{10\overline{1}0\}$ relrods, which are asymmetric about the center. At [0001] zone axis, the $\{11\overline{2}0\}$ planes scatter at higher intensity than the $\{10\overline{1}0\}$ planes. SAED tilt series for 1T WS_2 were also simulated and they appear very similar to 1T MoS_2 (not shown).

4. Discussion

The ADF-STEM image and SAED pattern simulation results are distinctly different from those obtained from graphene [40] or h-BN [29], most notably at the monolayer thickness: rather than scattering from a single plane of atoms, each of the three planes of atoms that form the MX_2 monolayer contribute to scattering as the electron beam in the TEM passes through the material. Whereas a h-BN monolayer and graphene produce approximate single scattering for such small tilt angles off of [0001], MX_2 monolayers produce plural scattering. Thus, tilting MX_2 of any thickness off of the [0001] zone axis affects the contrast of both ADF-STEM images and SAED patterns.

4.1. Distinguishing 2H and 1T polymorphs using ADF-STEM imaging

The ADF-STEM simulations show distinct differences between the 2H and 1T MoS_2 images, as expected from their different

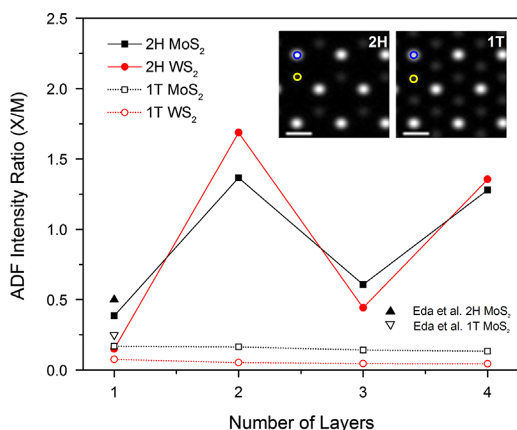

Fig. 4. ADF-STEM intensity ratios of X-site to M-site at [0001] zone axis for 1–4 layers of 2H MX_2 and 1T MX_2. Yellow dots represent the X-site and blue dots the M-site. 2H configuration alternates the higher intensity site as a result of the ABA-BAB stacking, whereas in 1T configuration with ABA-ABA stacking it remains constant (see also Fig. 1(c)). For comparison, experimental ADF-STEM image intensity ratios for 2H and 1T MoS_2 monolayers from ref. [26] are also shown. (For interpretation of the references to color in this figure legend, the reader is referred to the web version of this article.)

atomic arrangements. These simulated images are consistent with the experimental findings of Eda et al. [21], identifying 2H MoS_2 monolayers at [0001] zone axis as a honeycomb populated by visible M- and X-sites and 1T MoS_2 monolayers as a larger hexagonal structure of M-sites surrounded by undetectable X-sites. The ADF intensity from a X-site in a 1T crystal is less than half that in a 2H crystal because the 1T polymorph does not contain pairs of S atoms vertically aligned at the [0001] zone axis (see Fig. 1), leading to decreases in high-angle scattering. The results show that this distinction holds for all thicknesses of MoS_2. However, the intensity ratios of X- to M-sites in 1T at [0001] (see Fig. 4) show that the X-site still displays ~17% of the intensity of the M-site in MoS_2. Although noise in experimental ADF-STEM images may render the X-site undetectable, accurately processed images should in principle show the X-site since ADF scattering intensity from a single atom is detectable even for light atoms such as B, C and N and varies as $\sim Z^{1.5}$–$Z^{1.7}$ [41–43].

Although the same trends are observed for WS_2, X-site/M-site, ADF intensity ratios for 2H and 1T WS_2 monolayers are smaller in magnitude as ADF scattering from W ($Z_W = 74$) is far stronger than from Mo ($Z_{Mo} = 42$). For monolayers, the absolute difference between the ratios for the two polymorphs for WS_2 is less than 0.08 (or 8%) while for MoS_2 they differ by more than 0.2 (or 20%) (see Fig. 4). Thus, WS_2 monolayer polymorphs cannot be easily distinguished (using a conservative distinguishing criteria of greater than 10%) with evaluation of the X-site/M-site ADF intensity ratios from images recorded at [0001] zone axis; the W atoms will be clearly visible while the S atoms will be nearly undetectable in either case, as shown in Figs. 3 and 6. However, for 2 or more layers, 2H and 1T polymorphs of WS_2 can be distinguished. In the 2H polymorph, more comparable M-site and X-site ADF intensities are expected due to the additional W atoms in each atomic site.

In summary, for all thicknesses other than WS_2 monolayer, the high-intensity spots in the 2H polymorph are 1.8 Å apart while in the 1T they are 3.2 Å apart, a distinction easily observed in aberration-corrected STEMs.

4.2. Determining thickness with ADF-STEM imaging

4.2.1. Using relative intensities

A notable observation of the ADF-STEM imaging results for all the studied materials, except the 2H WS_2 monolayer, is that the layer count in practice cannot be unambiguously determined from image contrast at the [0001] zone axis alone. In the 2H polymorph the monolayer displays a lower X-site/M-site ADF intensity ratio than the multilayers (see Fig. 4), but since the brightest atomic column switches from M-site to X-site with odd and even number of layers, the distinction between thicknesses could still be ambiguous without additional support. This is in stark contrast to h-BN, where column-to-column intensity ratios can in principle be used to distinguish odd- and even-numbered layers [31].

The X-site/M-site ADF intensity ratios shown also indicate that in even-numbered layers there are appreciable intensity asymmetries between the M- and X-sites despite the identical compositions for all atomic columns. This phenomenon can be attributed to beam channeling [44–47]. As the beam propagates through the thin sample, each scattering center (atom) further focuses the beam. Since the high-angle scattering intensity from an atom depends on both its Z-number and the incident beam intensity distribution, the X-site, where the beam contacts the X atom first, shows higher intensity as the M atom further in the z-direction scatters a more focused (or intense) beam than the M atom above it at an adjacent M-site. Odd-numbered layers always have higher M-site intensity because they contain more M atoms. The 1T configurations do not display this behavior because M- and X-sites contain only their respective atoms in an atomic column at [0001] zone axis regardless of thickness. Instead, 1T layers display a weakly decreasing X-site/M-site ratio with increasing thickness. Extrapolating the trends of Fig. 4, it is expected at the bulk limit that M- and X-sites in 2H will be indistinguishable (X-site/M-site ≈ 1) while 1T will only display the M site (X-site/M-site $<< 1$).

Tilting the sample in the x or y directions alters atomic positions in the [0001] projection, as shown in Fig. 9 for an example of a 2H polymorph of MX_2. For very thin specimens (typically 1–3 layers thick) with small tilt angle ($<$ 100 mrad or $\sim 6^\circ$), when there is no overlap between adjacent columns, ADF-STEM images are roughly equivalent to projected structures of the crystal convoluted with the electron probe. However, when specimen thickness or tilt angle is large enough to cause overlap between neighboring atomic columns, such simplification is not accurate anymore and detailed image simulations are needed even to predict qualitative image contrast.

Using the intensity variation, it may be possible to identify the layer count by observing tilt-series trends during an experiment. For example, for the 2H polymorph, the shape of the higher intensity spots at 200 mrad x-tilt (or $\sim 12^\circ$) can distinguish samples 1, 2, 3 and 4 layers thick as shown in Fig. 2, Fig. 3 and Fig. 9 (b). Near this tilt, the M (Mo or W) atoms are separated from each other in projection and are also separated from the X (S) atom clusters. A periodic array of M atom clusters are then projected in a shape that is dependent on the number of M atoms present, or hence, the number of layers. For a monolayer, only a single M atom is observed in each M cluster, for the bilayer, the 2M atoms appear as a dumbbell, and 3- and 4-layer-thick samples form a triangle and a rhombus, respectively. At this tilt angle, the distance between clusters is ~2.5 Å and is easily resolvable with little interference from X atom clusters. At five or more layers, it is difficult to resolve the shapes since M atoms overlap within each cluster in this projection.

Distinguishing the number of layers is contingent on the ability to resolve the dominating M atom clusters and the shape of the clusters. Although other tilt angles and directions also produce unique intensity contrasts for each thickness (see Figs. 2, 3, 5 and 6), 200 mrad x-tilt off of the [0001] zone axis appears as a projection with the least stringent imaging conditions for both 2H and 1T polymorphs. As simulation results indicate, it is indeed possible to unambiguously verify the thickness of 2H and 1T MoS_2

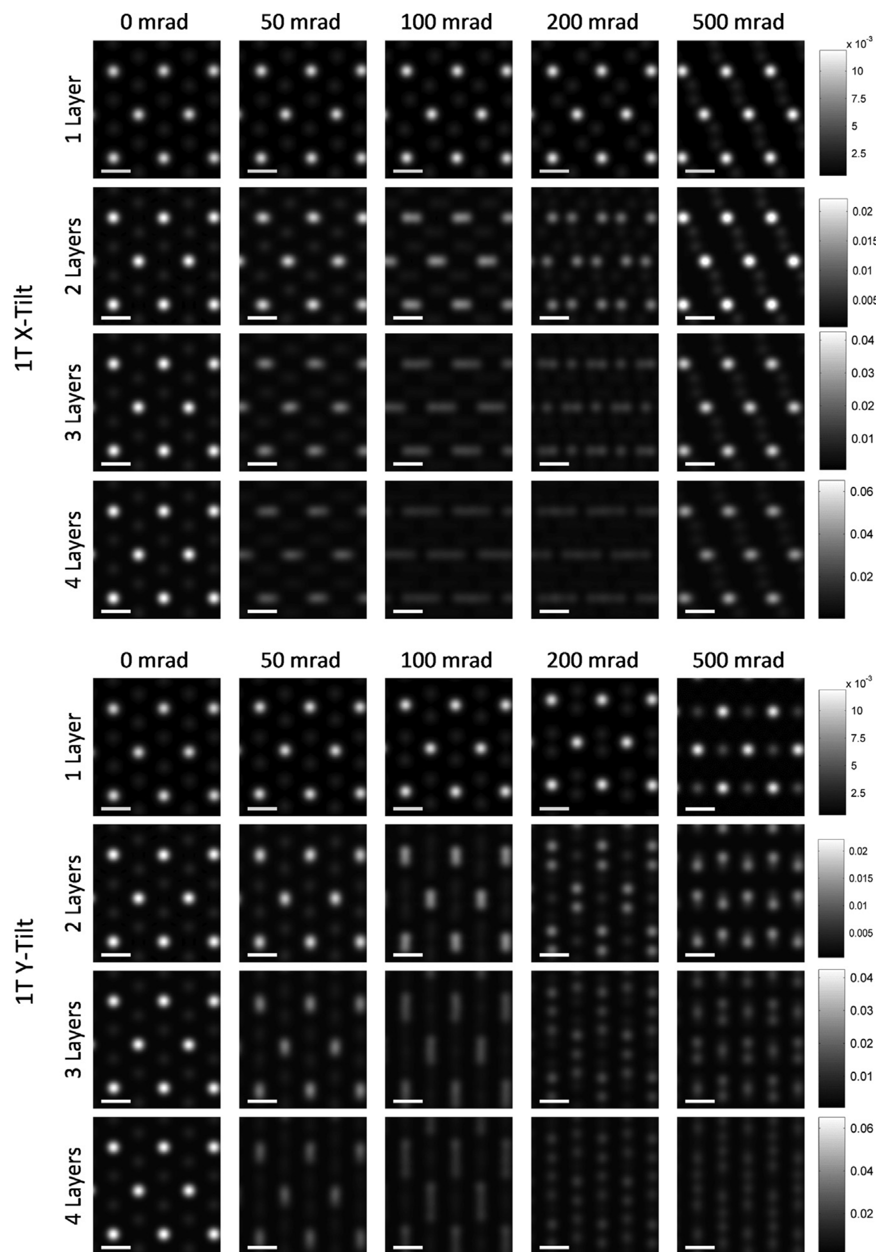

Fig. 5. Simulated ADF-STEM images of 1T MoS_2 at various *x*- and *y*-tilt angles. Both tilt directions produce unique intensity patterns at all thicknesses as a result of overlapping of Mo and S atoms. Color bars are scaled to each row with intensities normalized to the incident beam; scale bars are 1.8 Å.

and WS_2 up to 4 layers using relative intensities in ADF-STEM images by analyzing the shapes created by overlapping M atoms at 200 mrad of tilt about the *x*-axis for 2H polymorph, and about any axis for the 1T polymorph.

4.2.2. Using absolute intensities

Although relative intensities can be used for determining the number of layers of uniform sheets, situations may occur where an imaged area contains a step change in thickness. Because ADF intensity is sensitive to the atomic Z-number and the total number of atoms present in an atomic column, absolute intensities can be used to determine thickness provided that the ADF detector has been calibrated to measure the scattered electron current [22,48]. Fig. 10 shows ADF line intensity profiles for 2H and 1T MoS_2 and WS_2 samples simulated at [0001] zone axis. The intensities of both the M- and X-sites increase with thickness as additional atoms are added to each column. The different intensity jumps associated with adding an atom to the column at different depths can be attributed to beam channeling, as discussed in the previous section. Taking the highest intensity site as a reference, for both 2H and 1T polymorphs the number of layers can be discerned at least up to 4 layers. For example, for 2H MoS_2, the ADF intensity of the brighter site (which oscillates from M- to X-site and from X- to M-site with each additional layer) is: 0.01, 0.02, 0.03, and 0.05 for 1 to 4 layers respectively. This increase is roughly consistent with the experimental results of Zhou et.al [20]. The intensity increase is greater for 2H WS_2: 0.02, 0.04, 0.08, and 0.11 for 1 to 4 layers. The 1T polymorph, which keeps a constant high intensity M-site at any thickness, experiences larger increases in intensity with increase of number of layers than the corresponding 2H materials. This thickness dependence of peak intensity would allow

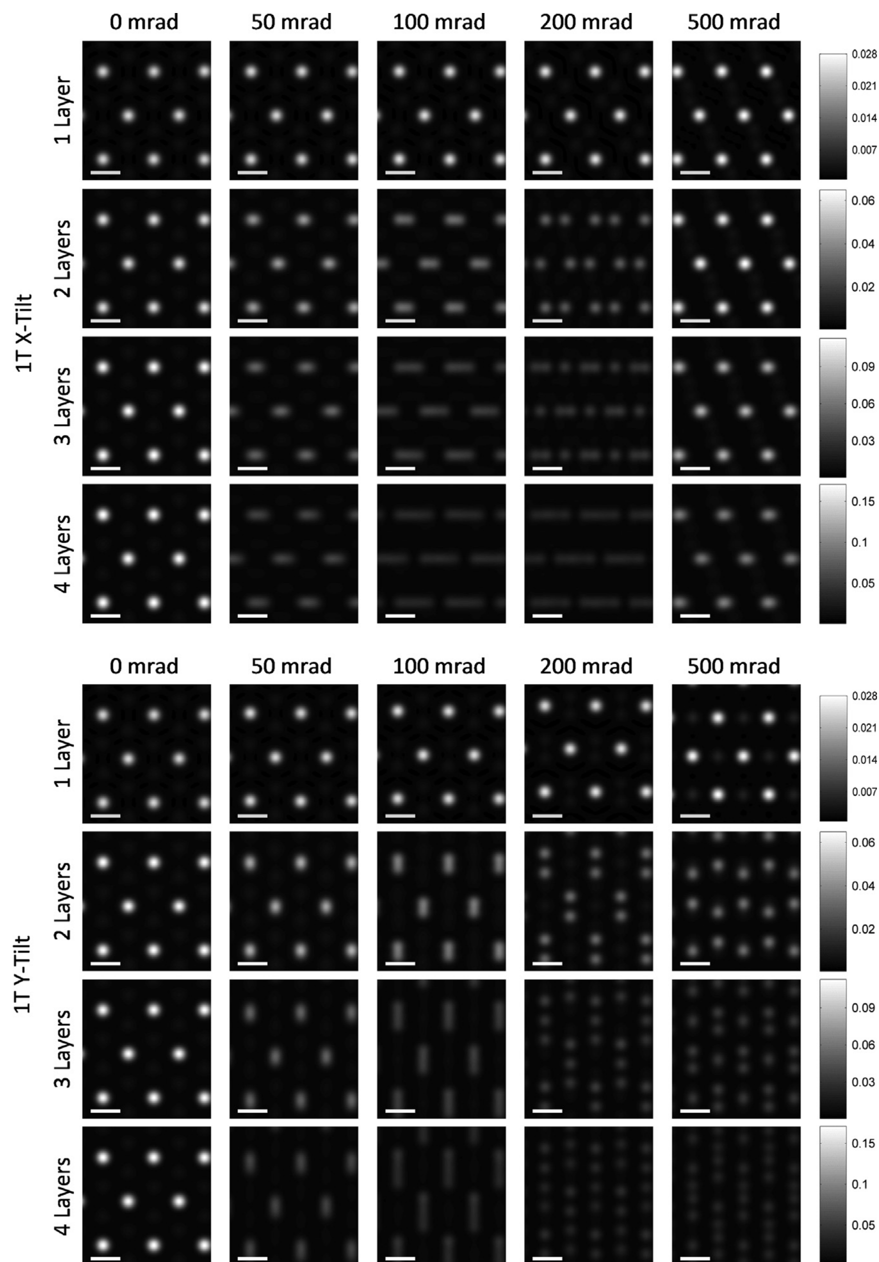

Fig. 6. Simulated ADF-STEM images of 1T WS_2 at various *x*- and *y*-tilt angles. Both tilt directions produce unique intensity patterns at all thicknesses as a result of overlapping of W and S atoms. Color bars are scaled to each row with intensities normalized to the incident beam; scale bars are 1.8 Å.

thickness determination as long as the ADF signal can be accurately quantified.

4.3. Distinguishing 2H and 1T polymorphs using SAED

SAED pattern simulations presented in Figs. 7 and 8 show that the 2H and 1T polymorphs (the results for WS_2 are not presented) exhibit similar diffraction spot positions but different intensities at the [0001] zone axis. Fig. 11 summarizes the ratios of the intensity of $\{10\overline{1}0\}$ spots to that of $\{11\overline{2}0\}$ spots for both materials and polymorphs at all four thicknesses. $\{10\overline{1}0\}$ spots in 2H polymorphs have ~75% the intensity of $\{11\overline{2}0\}$ spots for all four thicknesses. On the other hand, in 1T polymorphs $\{10\overline{1}0\}$ spots have only ~25% the intensity of $\{11\overline{2}0\}$ spots, again for all four thicknesses. This factor of 3 difference between 2H and 1T intensity ratios ($I_{10\overline{1}0}/I_{11\overline{2}0}$) that is observed for all four thicknesses can be used to distinguish the two polymorphs.

4.4. Determining thickness using SAED

The SAED simulations presented in Figs. 7 and 8 indicate that diffraction spots gain and lose intensity with tilt away from the [0001] zone axis in either direction for all thicknesses. By tracking the intensity of particular diffracted beams as a function of tilt angle as shown in Fig. 12, it can be seen that at every thickness, these TMD materials produce diffracted beams with clear intensity maxima and minima over the course of the 0–500 mrad tilt series. The fact that diffraction spots can vanish with sufficient tilt off of [0001] even for monolayers of MoS_2 and WS_2 distinguishes these TMD materials from truly planar graphene and h-BN monolayers [28,29,40].

To understand the origin of this difference between diffraction patterns of TMD and truly planar two-dimensional materials, we calculated the intensities of relrods for TMD materials. The results are presented in Fig. 13. For a layered material with a two-dimensional

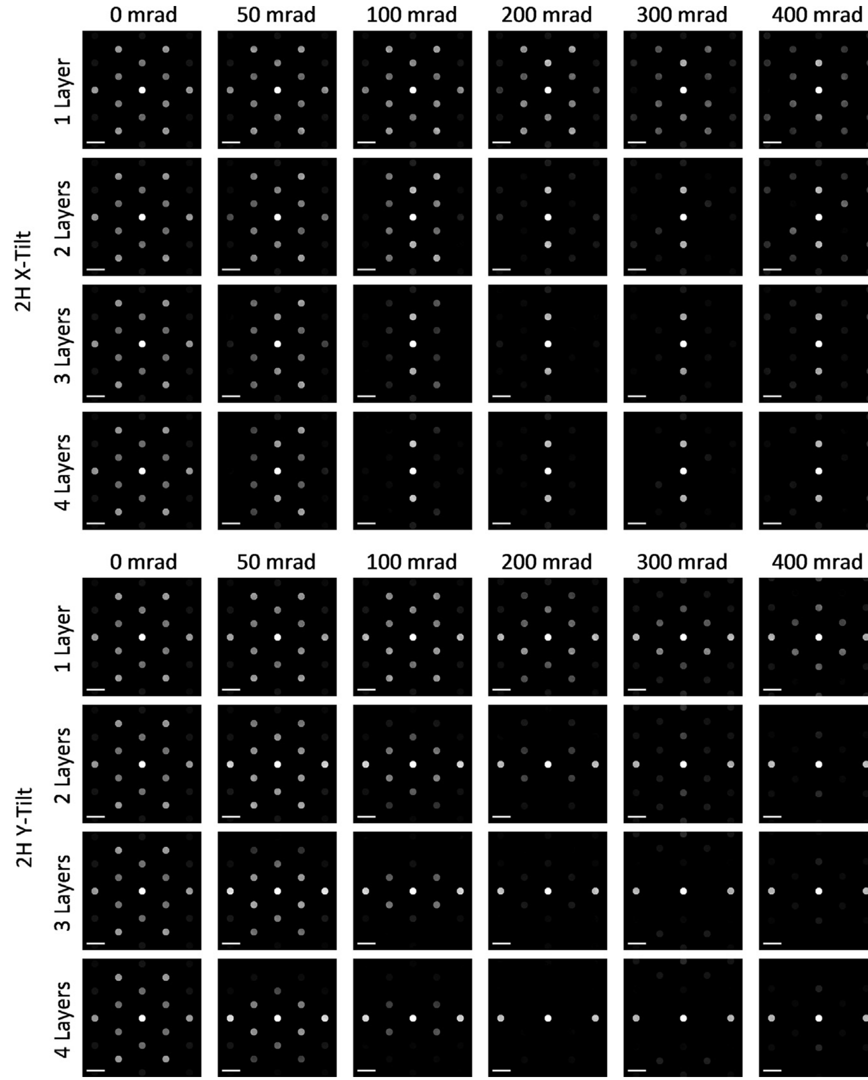

Fig. 7. Simulated SAED patterns of 2H MoS_2 at various *x*- and *y*-tilt angles. Both monolayer and multi-layer patterns contain diffraction spots that vanish with tilt, primarily for the band of spots perpendicular to the tilt axis. Linear intensity scaling; scale bars are 0.24 $Å^{-1}$.

unit cell defined in the x–y plane, the intensity, I, of a relrod as a function of the deviation of the reciprocal lattice point (in the zero-order Laue zone) from the Ewald sphere S_z, scattering vector $\boldsymbol{q}=\boldsymbol{g}+\boldsymbol{s}=g_x\hat{x}+g_y\hat{y}+S_z\hat{z}$, lattice amplitude factor G, and structure factor F, for an N-layer sample with z-spacing t can be expressed as [29,49]:

$$I(g_x,g_y,S_z)=\alpha\left|F(g_x,g_y,S_z)\right|^2\left|G(g_x,g_y,S_z)\right|^2$$
$$=\alpha'(g_x,g_y)\left|F(g_x,g_y,S_z)\right|^2\frac{\sin^2(\pi NtS_z)}{\sin^2(\pi tS_z)}, \quad (1)$$

where α and α' are proportionality constants. In planar crystals such as graphene or monolayer h-BN the structure factor depends on S_z only due to the decrease of atomic scattering factor amplitudes with increasing q. The variation in z position of the atoms in each TMD layer leads to an additional S_z dependence of structure factor due to the interference of the beams scattered from atoms within the layer. This accounts for why, even for TMD monolayers, $\{11\overline{2}0\}$ spots in 2H crystals and both $\{10\overline{1}0\}$ and $\{11\overline{2}0\}$ spots in 1T crystals disappear at sufficient tilt off of the [0001] zone axis.

Kinematic diffraction from TMD structures comprised of M and X atoms can be modeled by calculating the structure factor for electron scattering from a large-area TMD sheet. By treating the unit cell as three-dimensional rather than two-dimensional (the latter is inaccurate even for multilayers of graphene and h-BN due to the AB-type stacking of the atomic planes), and restricting the lattice amplitude G to solely treat tiling in the x–y plane of an "effective unit cell" 1–4 layers thick in z, the intensity of electron scattering to a relrod intersecting the Ewald sphere with scattering vector $\boldsymbol{q}$ can be calculated as:

$$F(g_x,g_y,S_z)=F(\boldsymbol{q})=\sum_i f_M(\boldsymbol{q})\,e^{2\pi i(\boldsymbol{q}\cdot\boldsymbol{r_i})}+\sum_j f_X(\boldsymbol{q})\,e^{2\pi i(\boldsymbol{q}\cdot\boldsymbol{r_j})} \quad (2)$$

$$I(g_x,g_y,S_z)=\alpha|F(g_x,g_y,S_z)|^2|G(g_x,g_y)|^2=\alpha'(g_x,g_y)|F(g_x,g_y,S_z)|^2 \quad (3)$$

$f_{\mathrm{M}}(q)$ and $f_{\mathrm{X}}(q)$ are the scattering factors for M and X atoms, respectively, and $\boldsymbol{r_i}, \boldsymbol{r_j}$ are the real space atomic position vectors. The calculated relrods are shown in Fig. 13 for $(10\overline{1}0)$ and $(1\overline{2}10)$ diffraction spots for both 2H and 1T samples, using parameterized atomic scattering factors [27]. The results of this model are also shown in Fig. 12, being transformed into a function of tilt angle by accounting for the geometry of crystal tilt relative to the Ewald sphere. The kinematic model correlates well with the results of the dynamical simulation, both agreeing on the intensity oscillations of each tracked spot as a function of tilt angle and specimen thickness. Slight discrepancies arise due to approximations made

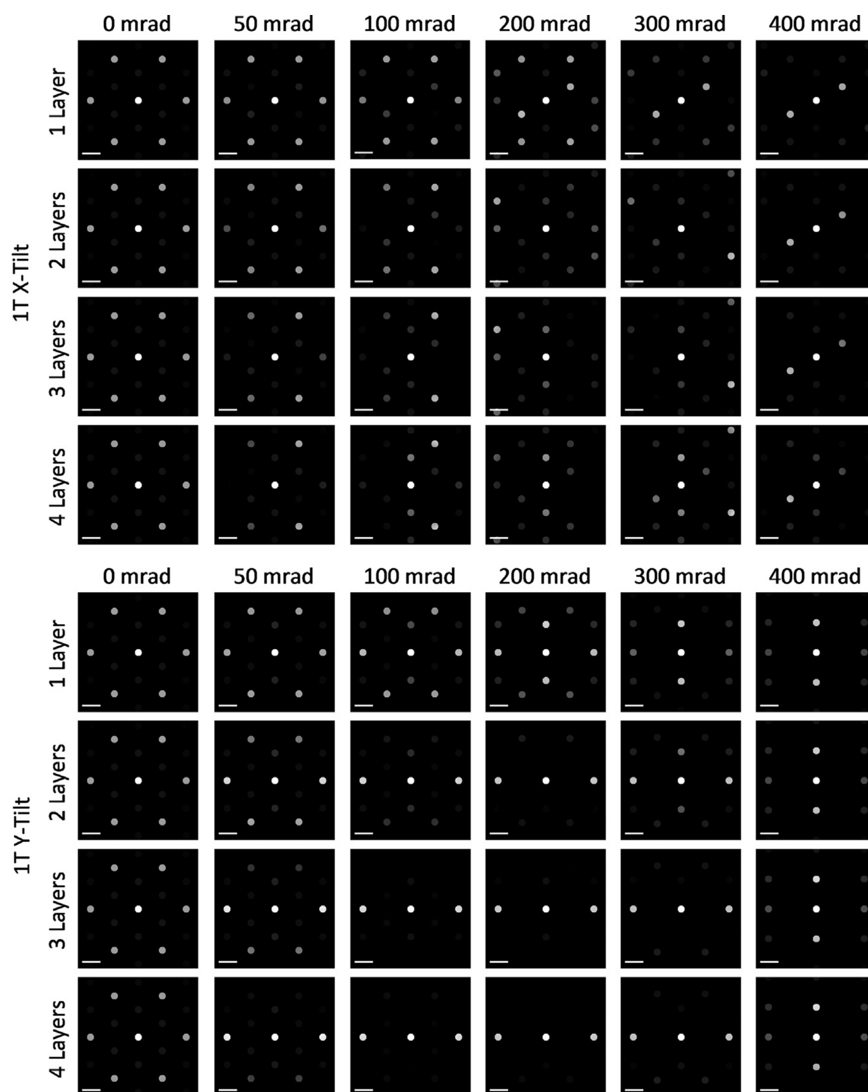

Fig. 8. Simulated SAED patterns of 1T MoS_2 at various *x*- and *y*-tilt angles. Both monolayer and multi-layer patterns contain diffraction spots that vanish with tilt, primarily for the band of spots perpendicular to the tilt axis. Linear intensity scaling; scale bars are 0.24 $Å^{-1}$.

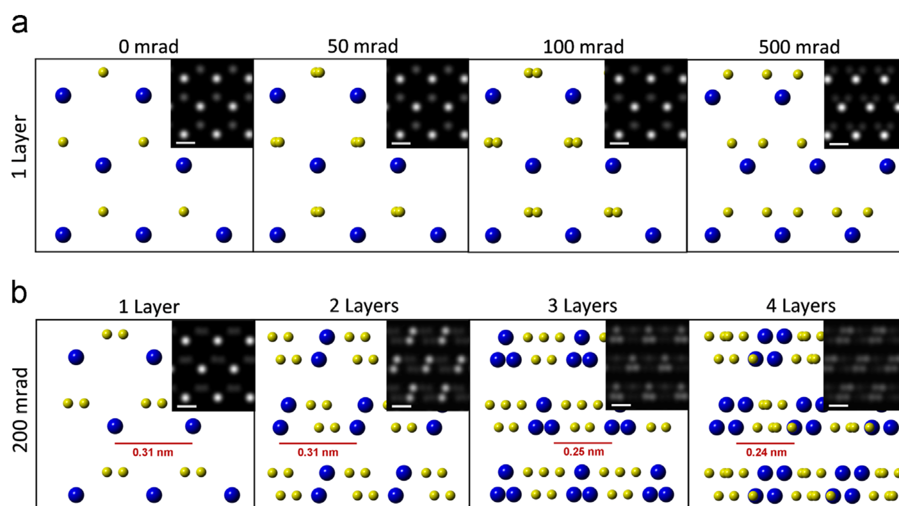

Fig. 9. Crystal model of the 2H polymorph of MX_2: (a) 1 layer MX_2 in [0001] projection tilted at different angles in *x*-direction, (b) 1 to 4 layers of MX_2 in [0001] projection tilted at 200 mrad in *x*-direction. Corresponding simulated ADF-STEM images of 2H MoS_2 are presented as insets.

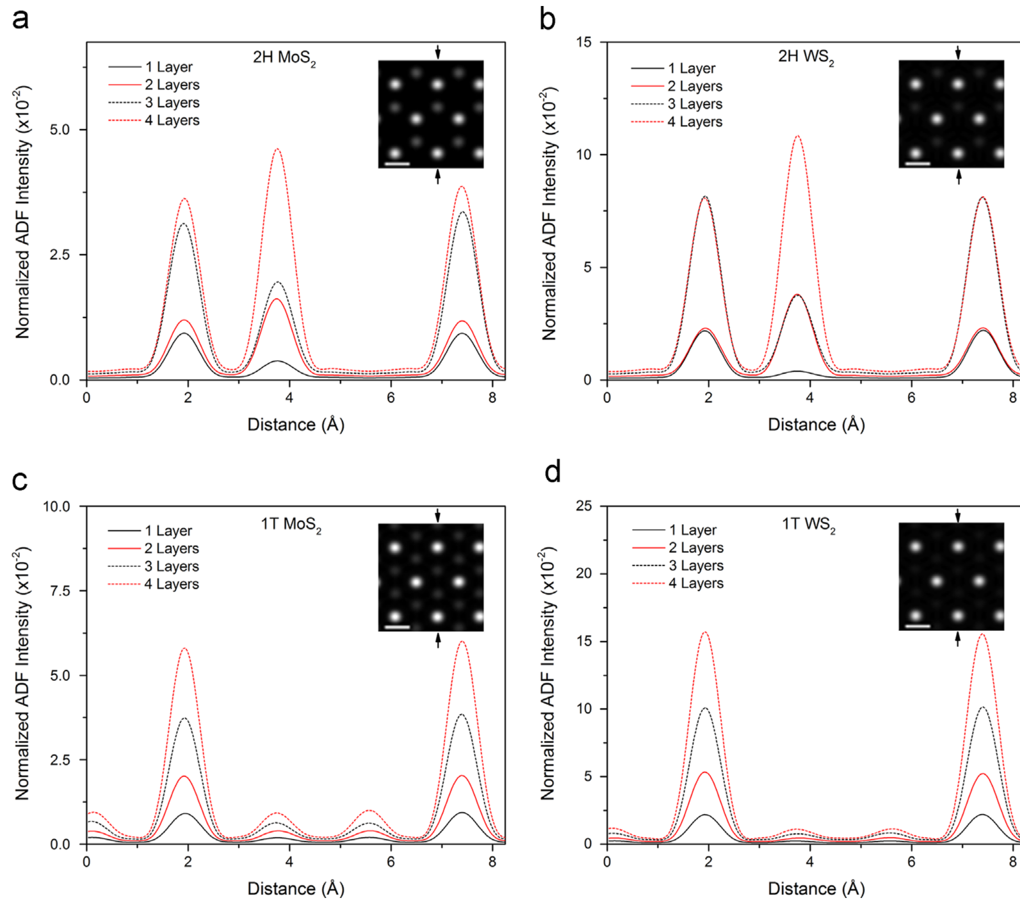

Fig. 10. Simulated ADF-STEM intensity linescans at [0001] zone axis: (a) 2H MoS_2; (b) 2H-WS_2; (c) 1T MoS_2; (d) 1T WS_2. Each line profile is 12 pixels (or 0.4 Å) averaged. The insets are corresponding ADF-STEM images with arrows indicating directions of linescans. Intensities are normalized to the incident beam.

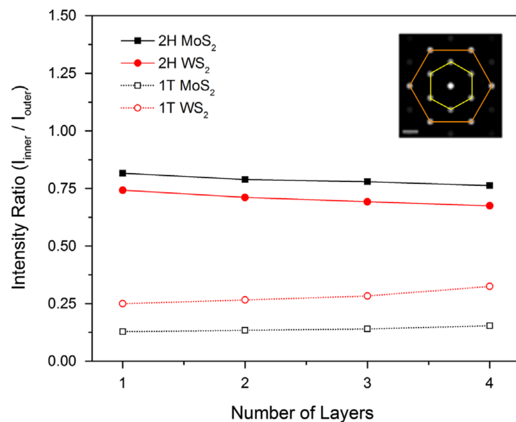

Fig. 11. Intensity ratios of $\{10\bar{1}0\}$ to $\{11\bar{2}0\}$ spots of [0001] zone axis SAED pattern simulated for both materials and polymorphs. The yellow and orange hexagon traces in the inset diffraction pattern are the two sets of spots that were used to evaluate the average $I_{10\bar{1}0}$ and $I_{11\bar{2}0}$. (For interpretation of the references to color in this figure legend, the reader is referred to the web version of this article.)

by the multislice simulation: the *z*-component of elastic scattering is ignored and atomic positions are distorted by projecting them onto the nearest *z*-slice.

Despite the fact that SAED pattern contrast is not tilt-invariant for TMDs, a monolayer and multilayer sample can still be distinguished, as also experimentally demonstrated by Brivio et al. [19] on 2H MoS_2: the intensity at the $(10\bar{1}0)$ spot for the monolayer retains most of its intensity at ~200 mrad tilt while for the bilayer it vanishes entirely. For 2H MoS_2 bilayer samples, the extinction of $(10\bar{1}0)$ spot at 200 mrad of tilt paired with an intensity maximum around 300–350 mrad should permit unambiguous identification of this thickness. 3- and 4-layer samples exhibit barely identifiable extinction of the $(10\bar{1}0)$ spots at tilts of ~150–175 mrad and ~100–125 mrad, respectively, followed by a second minimum in the 4-layer at 200–225 mrad. In addition, the $(10\bar{1}0)$ relrod (see Fig. 13) is symmetric about $S_z=0$. Thus, tilting in either the positive or negative direction will result in the same extinction behaviors. Applying the kinematic model and dynamical simulations to WS_2 (results are not included) shows that the behavior of the 2H WS_2 $(10\bar{1}0)$ spot is similar to that of 2H MoS_2.

Based on SAED results in Fig. 8, the same methods do not translate as well to 1T samples to discern the number of layers. One pair of $(10\bar{1}0)$ spots appear to begin with little intensity and gain intensity with tilt for all thicknesses, albeit interrupted by oscillations in intensity along the way to the 500 mrad peak value; this behavior is unique to 1T specimens and could be used to distinguish the two polymorphs from each other. For thickness determination, the high intensity of the $(10\bar{1}0)$ spot at 200 mrad *y*-tilt for the monolayer is a strong contrast from the almost vanishing behavior of the same spot for thicker samples, which is consistent with the intensity variations along the $(10\bar{1}0)$ and $(1\bar{2}10)$ relrods as shown in Fig. 13 (c) and (d). The relrods also show that bilayer and thicker samples do exhibit characteristic intensity variations as a function of tilt (extrema in the intensity oscillations of the $(10\bar{1}0)$ spots that increase in intensity with tilt and tilt-dependent behavior of the $(1\bar{2}10)$ almost identical to that of 1T), which may not be obvious from the diffraction patterns of Fig. 8.

Beyond distinguishing monolayers and bilayers from thicker samples, observing the relative tilt-series intensity in SAED does

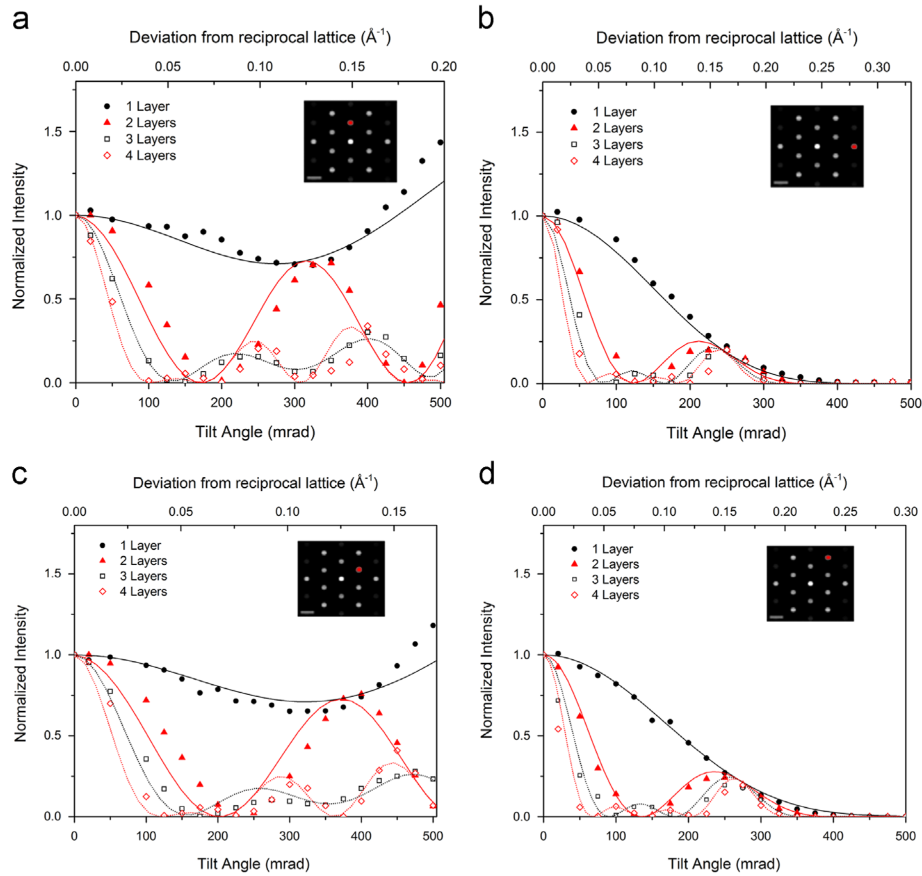

Fig. 12. SAED spot intensity variations as a function of tilt angle for 1 to 4-layered 2H MoS_2. The spot tracked in each plot is highlighted in red in the sample diffraction pattern. Scattered points represent simulated multislice data; solid lines represent the simple kinematic model. (a) $(10\bar{1}0)$ over *y*-tilt series. (b) $(1\bar{2}10)$ over *x*-tilt series. (c) $(1\bar{1}00)$ over *y*-tilt series (d) $(2\bar{1}\bar{1}0)$ over *x*-tilt series. Each simulated data point is a 12 × 12 average of the pixels surrounding the center of that diffracted spot. Intensity values are normalized to the averaged value at the [0001] zone axis. (For interpretation of the references to color in this figure legend, the reader is referred to the web version of this article.)

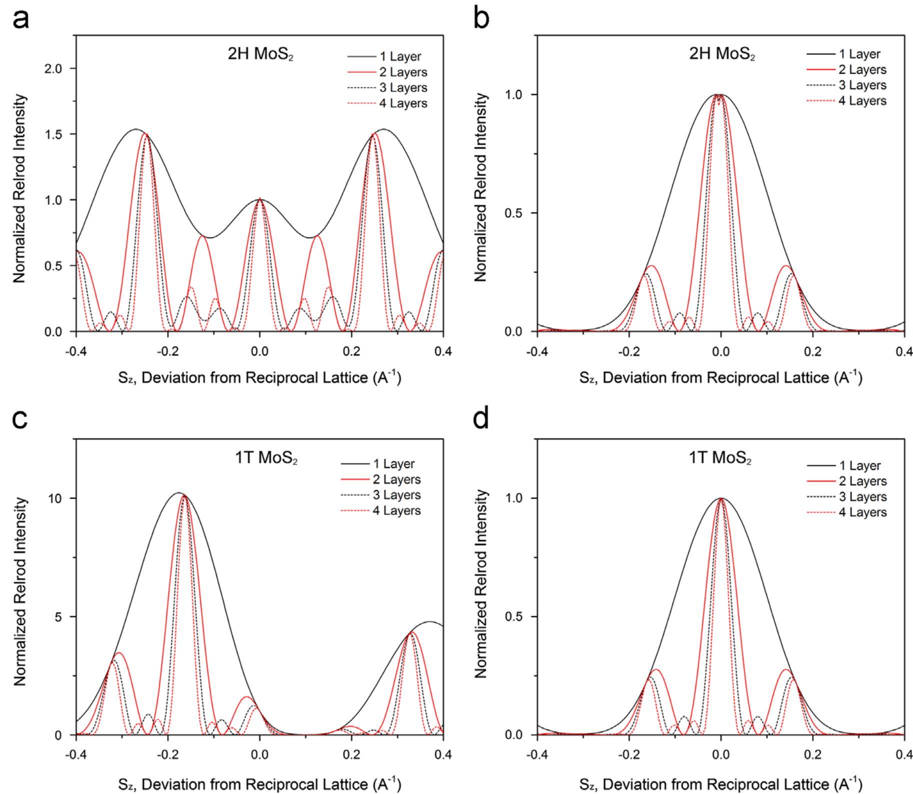

Fig. 13. Intensity variation along reciprocal space lattice rod: (a) $(10\bar{1}0)$ spot, 2H MoS_2; (b) $(1\bar{2}10)$ spot, 2H MoS_2; (c) $(01\bar{1}0)$ spot, 1T MoS_2; (d) $(1\bar{2}10)$ spot, 1T MoS_2. Plots are constructed using kinematic model. Intensity values are normalized to the value at $S_z = 0$.

not seem to be a practical means for measuring the thickness of TMDs; although simulations reveal signature behavior of 3- and 4-layer samples, these intensity variations are small and may be difficult to detect conclusively relative to those from monolayers and bilayers. Furthermore, the intensity variations of 3- and 4-layer samples are similar which makes thickness determination ambiguous. Successful use of this method would require a large area of sample with uniform thickness or a moderately converged beam that requires short exposure time to limit beam damage, neither of which is trivial to ensure. The use of these computational results also requires relatively accurate determination of the [0001] zone axis and tilt axis during experimental application. Because of the nearly two-dimensional nature of MX_2 TMD materials, 1- to 4-layer-thick flakes with reasonable lateral dimensions will likely be initially positioned near the [0001] zone axis when deposited on a standard TEM grid.

5. Conclusion

ADF-STEM and SAED simulations show that tilt effects are apparent when employing these TEM techniques for both 2H and 1T polymorphs of MoS_2 and WS_2 samples even at the monolayer thickness. Either technique can be reliably used with tilting off of zone axis [0001] to distinguish monolayer samples from multilayers, and in some cases distinguish different-thickness multilayers from each other. For ADF-STEM imaging, a resolution of $\sim$1 Å or better would be preferable. It appears that neither technique can unambiguously identify layer count solely based on relative intensity contrast at zone axis [0001], with the exception of monolayer 2H WS_2. However, layer differentiation is possible at zone axis [0001] using absolute intensities in ADF-STEM if the ADF signal is accurately quantified and compared to an equivalent simulation. In addition, the results showed that ADF-STEM and SAED could be also used to distinguish the 2H and 1T polymorphs of MoS_2 and WS_2 from each other.

Acknowledgments

This work was supported in part by C-SPIN, one of the six centers of STARnet, a Semiconductor Research Corporation program, sponsored by MARCO and DARPA and by the NSF under award number DMR-1006706, and the University of Minnesota Graduate School Fellowship. We also acknowledge receiving access to computational resources from the University of Minnesota Supercomputing Institute.

References

[1] A.K. Geim, K.S. Novoselov, The rise of graphene, Nat. Mater. 6 (2007) 183–191.
[2] Q.H. Wang, K. Kalantar-Zadeh, A. Kis, J.N. Coleman, M.S. Strano, Electronics and optoelectronics of two-dimensional transition metal dichalcogenides, Nat. Nanotechnol. 7 (2012) 699–712.
[3] M. Chhowalla, H.S. Shin, G. Eda, L.-J. Li, K.P. Loh, H. Zhang, The chemistry of two-dimensional layered transition metal dichalcogenide nanosheets, Nat. Chem. 5 (2013) 263–275.
[4] J.N. Coleman, M. Lotya, A. O'Neill, S.D. Bergin, P.J. King, U. Khan, K. Young, A. Gaucher, S. De, R.J. Smith, I.V. Shvets, S.K. Arora, G. Stanton, H.-Y. Kim, K. Lee, G.T. Kim, G.S. Duesberg, T. Hallam, J.J. Boland, J.J. Wang, J.F. Donegan, J. C. Grunlan, G. Moriarty, A. Shmeliov, R.J. Nicholls, J.M. Perkins, E. M. Grieveson, K. Theuwissen, D.W. McComb, P.D. Nellist, V. Nicolosi, Two-dimensional nanosheets produced by liquid exfoliation of layered materials, Science 331 (2011) 568–571.
[5] V. Nicolosi, M. Chhowalla, M.G. Kanatzidis, M.S. Strano, J.N. Coleman, Liquid exfoliation of layered materials, Science 340 (2013) 1226419.
[6] K.F. Mak, C. Lee, J. Hone, J. Shan, T.F. Heinz, Atomically thin MoS_2: a new direct-gap semiconductor, Phys. Rev. Lett. 105 (2010) 136805.
[7] K.K. Kam, B.A. Parkinson, Detailed photocurrent spectroscopy of the semiconducting group VI transitional metal dichalgogenides, J. Phys. Chem. 82 (1982) 463–467.
[8] A.R. Beal, H.P. Hughes, W.Y. Liang, The reflectivity spectra of some group VA transition metal dichalcogenides, J. Phys. C: Solid State Phys. 8 (1975) 4236.
[9] H. Li, Q. Zhang, C.C.R. Yap, B.K. Tay, T.H.T. Edwin, A. Olivier, D. Baillargeat, From bulk to monolayer MoS_2: evolution of raman scattering, Adv. Funct. Mater. 22 (2012) 1385–1390.
[10] Y. Yu, C. Li, Y. Liu, L. Su, Y. Zhang, L. Cao, Controlled scalable synthesis of uniform, high quality monolayer and layer MoS_2 films, Sci. Rep. 3 (2013) 1866.
[11] S. Najmaei, Z. Liu, W. Zhou, X. Zou, G. Shi, S. Lei, B.I. Yakobson, J.C. Idrobo, P.M. Ajayan, J. Lou, Vapour phase growth and grain boundary structure of molybdenum disulphide atomic layers, Nat. Mater. 12 (2013) 754–759.
[12] O.L. Krivanek, N. Dellby, A.J. Spence, R.A. Camps, L.M. Brown, Aberration correction in the STEM, Inst. Phys. Conf. Ser. 153 (1997) 35–40.
[13] M. Haider, S. Uhlemann, E. Schwan, H. Rose, K. Bernd, U. Knut, Electron microscopy image enhanced, Nature 392 (1998) 768–769.
[14] P.E. Batson, N. Dellby, O.L. Krivanek, Sub-angstrom resolution using aberration corrected eletron optics, Nature 418 (2002) 617–620.
[15] A.M. van der Zande, P.Y. Huang, D.A. Chenet, T.C. Berkelbach, Y. You, G.-H. Lee, T.F. Heinz, D.R. Reichman, D.A. Muller, J.C. Hone, Grains and grain boundaries in highly crystalline monolayer molybdenum disulphide, Nat. Mater. 12 (2013) 554–561.
[16] H.-P. Komsa, S. Kurasch, O. Lehtinen, U. Kaiser, A.V. Krasheninnikov, From point to extended defects in two-dimensional MoS_2: evolution of atomic structure under electron irradiation, Phys. Rev. B 88 (2013) 035301.
[17] R. Zan, Q.M. Ramasse, R. Jalil, T. Georgiou, U. Bangert, K.S. Novoselov, Control of radiation damage in MoS_2 by graphene encapsulation, ACS Nano 7 (2013) 10167–10174.
[18] K.S. Novoselov, D. Jiang, F. Schedin, T.J. Booth, V.V. Khotkevich, S.V. Morozov, A.K. Geim, Two-dimensional atomic crystals, PNAS 102 (2005) 10451–10453.
[19] J. Brivio, D.T.L. Alexander, A. Kis, Ripples and layers in ultrathin MoS_2 membranes, Nano Lett. 11 (2011) 5148–5153.
[20] W. Zhou, X. Zou, S. Najmaei, Z. Liu, Y. Shi, J. Kong, J. Lou, P.M. Ajayan, B.I. Yakobson, J.-C. Idrobo, Intrinsic structural defects in monolayer molybdenum disulfide, Nano Lett. 13 (2013) 2615–2622.
[21] G. Eda, T. Fujita, H. Yamaguchi, D. Voiry, M. Chen, M. Chhowalla, Coherent atomic and electronic heterostructures of single-layer MoS_2, ACS Nano 6 (2012) 7311–7317.
[22] H.E.K.E. MacArthur, T.J. Pennycook, E. Okunishi, A.J. D'Alfonso, N.R. Lugg, L.J. Allen, P.D. Nellist, Probe integrated scattering cross sections in the analysis of atomic resolution HAADF STEM images, Ultramicroscopy 133 (2013) 109–119.
[23] P.M. Voyles, D.A. Muller, J.L. Grazel, P.H. Citrin, H.-J.L. Gossman, Atomic-scale imaging of individual dopant atoms and clusters in highly n-type bulk Si, Nature 416 (2002) 826.
[24] J.M. LeBeau, S.D. Findlay, L.J. Allen, S. Stemmer, Position averaged convergent beam electron diffraction: theory and applications, Ultramicroscopy 110 (2010) 118–125.
[25] L.F. Kourkoutis, M.K. Parker, V. Vaithyanathan, D.G. Schlom, D.A. Muller, Direct measurement of electron channeling in a crystal using scanning transmission electron microscopy, Phys. Rev. B 84 (2011) 075485.
[26] R.F. Egerton, Electron Energy-Loss Spectroscopy in the Electron Microscope, 3rd ed., Springer, New York, 2011.
[27] T. Eberlein, U. Bangert, R.R. Nair, R. Jones, M. Gass, A.L. Bleloch, K.S. Novoselov, A.K. Geim, P.R. Briddon, Plasmon spectroscopy of free-standing graphene films, Phys. Rev. B 77 (2008) 233406.
[28] C.T. Pan, R.R. Nair, U. Bangert, Q. Ramasse, R. Jalil, R. Zan, C.R. Seabourne, A.J. Scott, Nanoscale electron diffraction and plasmon spectroscopy of single- and few-layer boron nitride, Phys. Rev. B 85 (2012) 045440.
[29] M.L. Odlyzko, K.A. Mkhoyan, Identifying hexagonal boron nitride monolayers by transmission electron microscopy, Micros. Microanal. 18 (2012) 558–567.
[30] J.M. Cowley, A.F. Moodie, The scattering of electrons by atoms and crystals, I. A New Theor. Approach, Acta Crystallogr. 10 (1957) 609–619.
[31] E.J. Kirkland, Advanced Computing in Electron Microscopy, 2nd ed., Springer, New York, 2010.
[32] M. Remskar, A. Mrzel, M. Virsek, M. Godec, M. Krause, A.S. Kolitsch, MoS_2 nanotubes with defect-controlled electric properties, Nanoscale Res. Lett. 6 (2010).
[33] Y. Shi, J. Huang, L. Jin, Y. Hsu, S.F. Yu, L. Li, H. Yang, Selective decoration of Au nanoparticles on monolayer MoS_2 single crystals, Sci. Rep. 3 (2013) 1839.
[34] J. Kang, S. Tongay, J. Zhou, J. Li, J. Wu, Band offsets and heterostructures of two-dimensional semiconductors, Appl. Phys. Lett. 102 (2013) 012111.
[35] A. Molina-Sanchez, L. Wirtz, Phonons in single-layer and few-layer MoS_2 and WS_2, Phys. Rev. B 84 (2011) 155413.
[36] J. Wen, J. Mabon, C. Lei, S. Burdin, E. Sammann, I. Petrov, A.B. Shah, V. Chobpattana, J. Zhang, K. Ran, J. Zuo, S. Mishina, T. Aoki, The formation and utility of sub-angstrom to nanometer-sized electron probes, Microsc. Microanal. 16 (2010) 183–193.
[37] A. Mittal, D.B. Zhang, C. Teresi, T. Dumitrica, K.A. Mkhoyan, Routes to identification of intrinsic twist in helical MoS_2 nanotubes by electron diffraction and annular dark-field scanning transmission electron microscopy imaging, Phys. Rev. B 84 (2011) 153401.
[38] J.L. Feldman, L.L. Boyer, Atomic mean-square displacements for 2H-MoS2, Solid State Commun. 37 (1981) 879–881.
[39] R.F. Loane, P. Xu, J. Silcox, Thermal vibrations in convergent-beam electron diffraction, Acta Crystallogr. Sect. A 47 (1991) 267–278.
[40] J.C. Meyer, A.K. Geim, M.I. Katnelson, K.S. Novoselov, T.J. Booth, S. Roth, The structure of suspended graphene sheets, Nature 446 (2007) 60–63.

[41] K. Suenaga, M. Koshino, Atom-by-atom spectroscopy at graphene edge, Nature 468 (2010) 1088–1090.
[42] Q.M. Ramasse, C.R. Seabourne, D.-M. Kepaptsoglou, R. Zan, U. Bangert, A.J. Scott, Probing the bonding and electronic structure of single atom dopants in graphene with electron energy loss spectroscopy, Nano Lett. 13 (2012) 4989–4995.
[43] O.L. Krivanek, M.F. Chisholm, V. Nicolosi, T.J. Pennycook, G.J. Corbin, N. Dellby, M.F. Murfitt, C.S. Own, Z.S. Szilagyi, M.P. Oxley, S.T. Pantelides, S.J. Pennycook, Atom-by-atom structural and chemical analysis by annular dark-field electron microscopy, Nature 464 (2010) 571–574.
[44] J. Fertig, H. Rose, Resolution and contrast of crystalline objects in high-resolution scanning transmission electron microscopy, Optik 59 (1981) 407–429.
[45] R.F. Loane, E.J. Kirkland, J. Silcox, Visibility of single heavy atoms on thin crystalline silicon in simulated annular dark-field STEM images, Acta Crystallogr. A 44 (1988) 912–927.
[46] P.M. Voyles, D.A. Muller, E.J. Kirkland, Depth-dependent imaging of individual dopant atoms in silicon, Microsc. Microanal. 10 (2004) 291–300.
[47] A. Mittal, K.A. Mkohyan, Limits in detecting an individual dopant atom embedded in a crystal, Ultramicroscopy 111 (2011) 1101–1110.
[48] J.M. LeBeau, S. Stemmer, Experimental quantification of annular dark-field images in scanning transmission electron microscopy, Ultramicroscopy 108 (2008) 1653–1658.
[49] L. Reimer, H. Kohl, Transmission Electron Microscopy, 5th ed., Springer, New York, 2008.